ACS OMEGA

Open Access

http://pubs.acs.org/journal/acsodf

Article

Quantifying Monomer−Dimer Distribution of Nanoparticles from Uncorrelated Optical Images Using Deep Learning

Abu S. M. Mohsin* and Shadab H. Choudhury

Cite This: *ACS Omega* 2025, 10, 862−870

Read Online

ACCESS | Metrics & More | Article Recommendations | Supporting Information

ABSTRACT: Nanoparticles embedded in polymer matrices play a critical role in enhancing the properties and functionalities of composite materials. Detecting and quantifying nanoparticles from optical images (fixed samples—in vitro imaging) is crucial for understanding their distribution, aggregation, and interactions, which can lead to advancements in nanotechnology, materials science, and biomedical research. In this article, we propose an ensembled deep learning approach for automatic nanoparticle detection and oligomerization quantification in a polymer matrix for optical images. The majority of prior studies of nanoparticle identification and categorization of fixed samples are based on scanning electron microscopy (SEM) or transmission electron microscopy (TEM) images, which are destructive to biological imaging. However, the proposed study is based on optical images, which are susceptible to noise, low contrast, anisotropic shape, overlapping of the point spread function, plasmon coupling, and resolution limitations. In this study, we fine-tune a deep neural network architecture, YOLOv8, on a carefully annotated data set of correlated optical and SEM images of 80 nm gold nanospheres (AuNSs) of varying oligomerization states. The resultant model features a weighted average accuracy of 80.7% for quantification of AuNSs and determination of their oligomeric state, far surpassing the capabilities of existing manual image processing methods. We also demonstrate its speed and effectiveness in nanoparticle detection and oligomerization within the polymer matrix through tests on high-density uncorrelated optical images. The optical image-based quantification technique will be useful for (live samples—for in vivo imaging) analyzing nanoparticle uptake, oligomerization state, and aggregation kinetics in live cells and identifying stoichiometry of membrane protein and its interactions, nanoparticle−cell interaction, cell signaling imaging, and drug delivery.

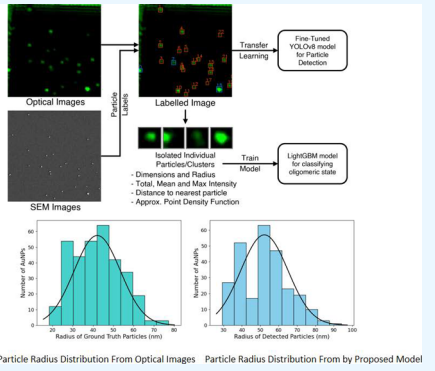

1. INTRODUCTION

Gold nanoparticles (AuNPs) play a significant role in various fields, including drug delivery, imaging, solar cells,[1−3] disease detection and sensing,[3,4] nanoantenna design,[5] etc. The localized surface plasmon resonance and field enhancement are typically dominated by nanoparticle size, shape, geometry, environment, and oligomerization state.[3,6]

While there has been extensive research on the characterization and analysis of nanoparticles, particularly focusing on their optical properties, the quantification of monomer−dimer distributions using uncorrelated optical images remains underexplored due to the unavailability of appropriate tools and resolution limitations.

The resolution limit of the optical technique is limited by the diffraction limit, which can be described by Rayleigh's criteria. This can be determined by the wavelength of light, which determines the minimum resolvable distance between two point sources by the following equation $d = 0.61\lambda/\mathrm{NA}$. Here, d is the minimum resolvable distance, λ is the wavelength of light, and NA (numerical aperture) is a measure of the lens's ability to gather light and resolve fine specimen detail.

For visible light (400−700 nm wavelength), the theoretical spatial resolution limit is 200−300 nm for conventional microscopy. The resolution is directly affected by wavelength: shorter wavelength (e.g., ultraviolet light) can provide higher resolution, whereas longer wavelength (e.g., infrared) yields lower resolution.

Scanning electron microscopy (SEM) and transmission electron microscopy (TEM) offer high-resolution images for nanoparticle morphology (fixed samples—in vitro imaging) but encounter challenges with biological samples (live samples—in vivo imaging) due to the complexity of sample preparation, high vacuum requirements, and the need for fixation and dehydration.

There are some solutions for this. For instance, Okada and Ogura[7] demonstrated scanning-electron-assisted dielectric

Received: August 28, 2024
Revised: December 2, 2024
Accepted: December 4, 2024
Published: January 3, 2025

microscopy (SE-ADM), which allows for high-contrast, high-resolution imaging of untreated living mammalian cells under physiological conditions, significantly reducing radiation damage while clearly visualizing cells and organelles without staining.

In another recent study,[8] Ogura and co-workers used SE-ADM to reveal the state and organization of proteins in unlabeled living cells (MNT-1 cells). The proposed SE-ADM is described as a useful tool for prescreening fixed biological specimens.

However, these methods are not perfect. Many biological samples have autofluorescence capabilities, which complicate the imaging process.[3] Additionally, overlapping fluorescence from multiple sources can lead to difficulty in distinguishing closely spaced particles. Biological tissues and cells can scatter light, which can further degrade the resolution and hinder the ability to obtain clear images. Optical lenses may introduce aberrations, such as spherical aberration or chromatic aberration, which can distort images and further limit resolution. With high numerical aperture lenses, the depth of field decreases, making it challenging to focus on thin layers or structures within thicker specimens. Prolonged exposure to excitation light can cause fluorescent dyes or proteins to lose their ability to emit light, making it difficult to maintain clear and consistent imaging over time. For weakly scattering or fluorescent samples, obtaining sufficient contrast can be a challenge, affecting the ability to differentiate between different structures.

For general imaging, confocal laser scanning microscopy[3] or dark-field confocal scattering microscopy[4] is often preferred for general biological imaging due to its ease of use, speed, sectioning capabilities, fluorescent probes' compatibility and ability to handle larger samples. Moreover, it can provide high-resolution images while minimizing photobleaching and phototoxicity, which are critical for observing living cells over time.[3]

However, for high-resolution imaging to investigate molecular interactions or small structures within cells, super-resolution microscopy would be a better option. Super-resolution microscopy (e.g., STED, PALM, and STORM) can achieve resolutions beyond the diffraction limit, often down to tens of nanometers.

Traditional methods typically rely on correlated measurements, such as electron microscopy or correlated light scattering techniques, which are time-consuming and require sophisticated instrumentation. Furthermore, current optical methods often fall short of providing a direct and efficient quantification of the monomer−dimer distribution due to limitations in resolving closely spaced nanoparticles and distinguishing between different aggregation states. This gap highlights the need for a method that can accurately quantify the distribution of monomers and dimers in nanoparticle samples by using simpler, more accessible optical techniques.

Identifying nanoparticles in a polymer matrix and determining their aggregation state from optical images is challenging due to the low contrast, anisotropic shape, overlapping particle instances, and resolution limits.[3,9]

Though fluorescence or transmission electron microscopy can provide quantitative information, further analysis usually relies on manual processing or human expertise, which can be inaccurate and inefficient. SEM/TEM imaging could be useful for dielectric/plasmonic random medium samples/fixed samples.[3,4] However, it becomes destructive when used for biological samples, including nanoparticle-attached live cells due to high radiation exposure, which damages cellular components and alters their morphology. The high-energy electrons can lead to heating, ionization, and other processes that can destroy delicate biological features. SEM requires a high vacuum environment to operate effectively. Biological samples, such as cells, may dehydrate and collapse under vacuum conditions, further complicating imaging and potentially leading to a loss of structural integrity. To prepare cell samples for SEM, they often need to be coated with conductive materials (such as gold or platinum) to prevent charging from the electron beam. This coating process can alter the sample and render it nonviable for further biological analysis.

In contrast, dark-field confocal optical imaging uses visible light and does not require a vacuum environment. This type of imaging is generally nondestructive as it examines light scattered from the sample rather than bombarding it with high-energy electrons. As a result, it preserves the biological structures and allows for the observation of live-cell dynamics without the damaging effects associated with electron beams. Therefore, dark-field scattering microscopy is preferred more for live cell imaging. However, specifically when nanoparticles are attached and/or incubated with cells, they are engulfed by the cell membrane. In that case, identifying NP oligomerization from TEM images is not possible, and optical (dark field confocal) may be more effective.

Recently, many semiautomatic computer-aided microscopy image processing tools, such as ImageJ or cisTEM, require an extensive user setup for image processing, such as selecting specific thresholds or filter properties. Due to the ever-increasing volume of experimental data, a quick and effective method for quantitatively extracting the total number of NPs and their aggregation state from optical images is critical.

Compared to scanning electron microscopy or tunneling electron microscopy imaging, optical images have several advantages such as being usable for in situ studies, being nondestructive, and having higher throughput, lower cost, and greater accessibility, especially for in vivo imaging.[10]

However, optical images suffer from many more issues compared with the crisp clear images returned by SEM or TEM. In optical images, particles of the same size may have inconsistent visible diameters. They tend to be present at varying distances from the microscope, making it challenging to focus on all of the particles in view. Reflections off the imaging surface can create bright lines and blurs around the edges of the images. The point spread function (PSF) of particles in the optical image will be identical due to nanoparticle plasmon coupling. The PSF of each particle is also much larger and brighter, causing distinct particles to blur together.

An oligomer with clearly distinct particles in an SEM or TEM image can appear as a single bright blob in an optical image. Additionally, the angle of polarization can have an effect on the overall intensity distribution. Data points, such as the quantum yield (dimer to monomer intensity ratio) and PSF, are also unavailable in optical images.

Previous studies on nanoparticle quantification have been done mostly on SEM or TEM images[11−13] on dielectric medium. Little to no quantification work regarding oligomerization has been done on optical images (live cell imaging) due to the complexity and randomness of the emitters, as well as the myriad challenges described above.

https://doi.org/10.1021/acsomega.4c07914
ACS Omega 2025, 10, 862−870

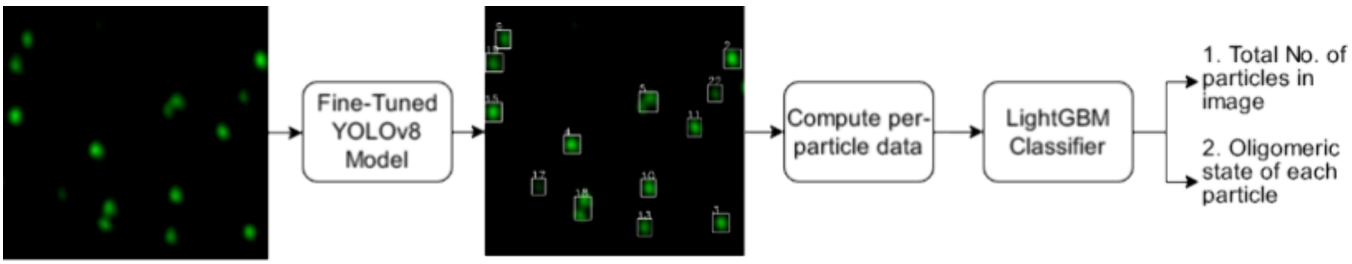

Figure 1. Summary of the proposed method: Performing inference on fine-tuned YOLOv8, computing particle data, employing a light GBM classifier model, and estimating the total number of particles and oligomeric state within optical images.

In this article, we describe a method for automating the nanoparticle counting process and identifying the oligomeric state in optical images using deep learning on images of gold nanospheres. Deep learning allows us to analyze optical images and extract quantitative data regarding the particles. SEM images are used as a ground truth for comparison. This is a novel method that achieves high accuracy for particle detection and classification on optical microscopy images, comparable to that for SEM images. Here, Figure 1 gives an overview of how the counting process works and the steps involved.

The novelty of this study lies in its approach to quantifying the monomer−dimer distribution of nanoparticles using uncorrelated optical images. Unlike previous methodologies that rely on complex, correlated imaging techniques, this paper proposes a method that leverages uncorrelated optical data, which is more straightforward and potentially scalable for high-throughput analysis. The study introduces innovative image processing algorithms and analysis techniques that enhance the ability to distinguish and quantify monomers and dimers directly from optical images in a nondestructive setting. This approach could significantly reduce the complexity and cost associated with nanoparticle characterization, making it accessible to a broader range of applications in nanotechnology, materials science, and biomedical research.

2. BACKGROUND

While the use of deep learning has been extensively studied in cell segmentation, cell imaging, and other types of microscopies, it is still a developing field when it comes to applications in nanoparticle detection and oligomerization analysis.

One challenge in the field is the wide variety of imaging modalities, such as optical, SEM, TEM, and so forth, each of which gives very different outcomes in terms of visual features. Domain adaptation and transfer learning can be used to overcome this issue, but there are inevitable falloffs in accuracy. Therefore, models and methods that are specialized for each imaging modality are required.

Traditional methods, such as geometric analysis and edge detection,[11,14] have been extensively studied and implemented in existing computer-aided microscopy tools and software like ImageJ[15] or CisTEM. However, these approaches are not as accurate and often fail when challenged by images featuring dense clustering, occlusion, etc. Deep learning approaches can resolve these issues.

Most prior work applying deep learning in this field has been focused on SEM and TEM imaging. The reason for this is obvious—those images are very easy to process and model and do not face the challenges that optical images do. Qu et al.[16] used a YOLO v5 convolutional neural network (CNN) model to quantify NPs of size ranging from 11 to 50 nm from TEM images. However, they were able to extract only position and diameter information from the particles, which is not enough to extract the oligomeric state. Oktay and Gurses[13] achieved an F1 score of 0.98 on detecting distinct particles in TEM images but did not carry out any further analysis. Dahy et al.[12] achieved a similar 0.98 F1 score on palladium nanoparticles in SEM images. Similar or weaker results were seen in refs 17−21, using a variety of different CNN models, different nanoparticles, and either SEM or TEM images.

On the other hand, most work on optical images focus on the micrometer scale—cells and their components.[22] However, some limited studies of optical images of nanoparticles do exist. Xu[23] used deep learning on optical images of silver NPs but focused on individual particles rather than collections. They predicted morphologies with an accuracy of 82%. Mohsin and Choudhury[24] showed that gold nanoparticles can be accurately counted from optical images, but extracting additional information like their oligomeric state or interparticle distance remains challenging.

Our work is novel in the sense that we focus on NP detection, aggregation, and oligomerization in optical images for in vitro imaging. There has been very little prior research on this type of analysis of optical images compared with SEM or TEM images. The findings of this study will pave the way for studying molecular interactions at the nanoscale from optical images, especially for in vivo imaging.

3. METHODOLOGY

The methods section is divided into two steps—preprocessing the data set and training the model.

Because of the lack of data for higher-order nanoparticles, it is difficult to achieve accurate results purely from an object detection model. Therefore, we use an ensemble approach—first, detecting the bounding box of each nanoparticle using the object detection model and then extracting spatial and pixel-wise features from it to classify the type of particle as a monomer or oligomer using another machine learning model. A link to the code is given in Supporting Information Section 1 (Link to Code).

3.1. Data Sets and Preprocessing. We initially began with a small data set of 8 pairs of optical (confocal laser scattering) images of 80 nm diameter gold nanospheres (AuNSs) and their correlated SEM images. The SEM images provide the ground truth for the exact number of particles, as well as their oligomeric state needed to train the models.

It is difficult to capture the optical image and its correlated SEM imaging simultaneously. The positions of the particles in the ground truth SEM images were slightly shifted with respect to the corresponding particles in the optical image. Each paired

https://doi.org/10.1021/acsomega.4c07914
ACS Omega 2025, 10, 862−870

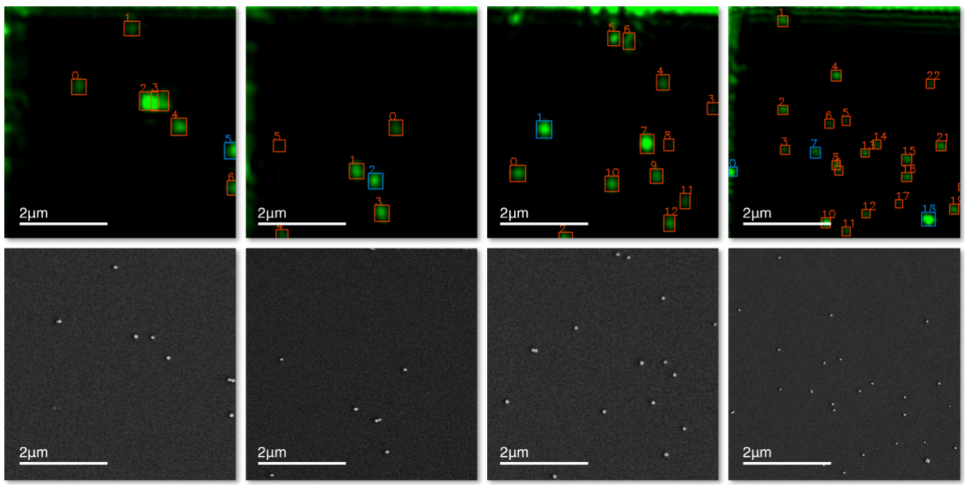

Figure 2. Top—Samples of training and validation images with bounding boxes labeled. Red indicates a monomer, and blue indicates an oligomer. Bottom—Corresponding ground truth SEM images.

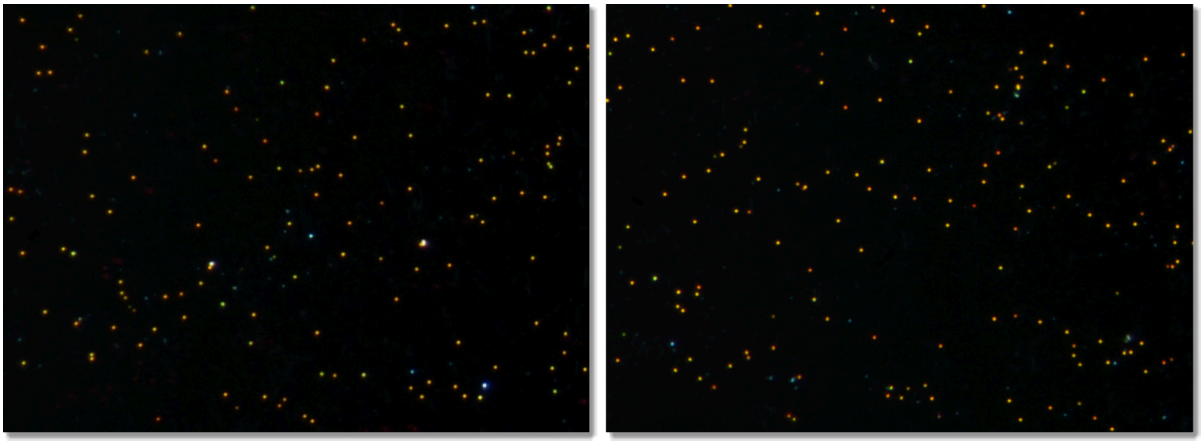

Figure 3. Examples of uncorrelated white-light excited images. The left and right images are dark-field confocal scattering images of the same sample (AuNSs of 80 nm diameter) imaged at two different locations. These images are much larger—2560 × 1920 pixels.

optical and SEM image was manually aligned before labeling. For labeling and counting particles in the SEM image, ImageJ's particle counter was used; however, it is also easy to label particles from the SEM image by hand.

We take seven of these images as our training set and one as our validation set. Extensive preprocessing is carried out at the batching step, and every batch has a random set of training and validation images. Therefore, the model does not actually see any of the original images, just the processed images. We are then able to use the original data set as a correlated test set without any data leakage. For the uncorrelated test set, we use a set of 20 optical images of white-light excited gold nanoparticles (AuNPs) that have no corresponding SEM image. Figure 2 shows the training/validation set with bounding boxes labeled along with corresponding SEM images, and Figure 3 shows a sample of the uncorrelated test set. Nanoparticle sample preparation and imaging details are given in Supplementary Section 2 (Preparing Gold Nanospheres for Imaging).

3.1.1. Detection and Counting. For detection and counting purposes, each particle in the training and validation sets was manually labeled using a bounding box and an oligomeric state label. Due to the low representation of higher oligomeric states, such as trimers and tetramers, we used binary-state labels of monomer and oligomer instead.

Extensive image augmentation was used to extend the limited data set for detection and counting. For photometric augmentations, we use randomized color jitter, sharpen, and Gaussian blur. For spatial augmentations, we use horizontal and vertical flips and randomized resizing crops (cropping out a random part of the image and resizing it).

3.1.2. Classification of Oligomers. The data for the spatial and pixel-wise features of our oligomeric state classifier are extracted from the original ground truth bounding box labels. We extract the following features from each bounding box encompassing a nanoparticle: radius, which is half the diagonal of the bounding box, center point $p(x_c, y_c)$ (eq 1), maximum intensity i_{max} (eq 2), total intensity i_{tot} (eq 4), average intensity $\hat{i}$ (eq 5), Euclidean distance to nearest particle d_n, and pixel point density function $p_{px}(x, y)$ expressed as a two-dimensional Gaussian (eq 6). The equations are given as follows:

$$p(x_c, y_c) = \left(x_0 + \frac{w}{2}, y_0 + \frac{h}{2}\right) \tag{1}$$

where (x_0, y_0) is the coordinate of the top left corner of the bounding box and w and h are the width and height of the box, respectively.

https://doi.org/10.1021/acsomega.4c07914
ACS Omega 2025, 10, 862−870

$$i_{\max} = \max(F[x_{bb}, y_{bb}]) \tag{2}$$

$$F[x_{bb}, y_{bb}] = F[[x_0, x_0 + w], [y_0, y_0 + w]] \tag{3}$$

where $F[x_{bb}, y_{bb}]$ represents the set of pixel intensity values for each pixel coordinate within the area of the bounding box.

$$i_{\text{tot}} = \sum_{x=x_0}^{x_0+w} \sum_{y=y_0}^{y_0+w} F[x_{bb}, y_{bb}] \tag{4}$$

For the total intensity, the pixel intensity values of each pixel coordinate within the bounding box are summed up.

$$\hat{i} = \frac{i_{\text{tot}}}{wh} \tag{5}$$

For the average pixel intensity, we simply divided the total intensity by the area of the bounding box.

$$p_{\text{px}}(x, y) = \frac{1}{2\pi\sigma_x\sigma_y} e^{-\left(\frac{x_c^2}{2\sigma_x^2} + \frac{y_c^2}{2\sigma_y^2}\right)} \tag{6}$$

Finally, to compute the pixel point density function, we use the two-dimensional Gaussian function, where σ_x and σ_y are the standard deviations in the x-axis and y-axis, respectively, with the mean located at the center point of the bounding box. The maximum value of the kernel is clamped to the maximum intensity of the particle.

For each bounding box, we compute σ_x and σ_y through gradient descent and pixel-wise mean square error loss. We used a learning rate of 0.01 and updated the values for 100 iterations. While it is difficult to generate a Gaussian that approaches the original particle in terms of shape and intensity due to their irregular blob-shaped appearances due to variation of excitation source and polarization, the Gaussian approximates the particle's total intensity. Brighter particles will have larger values of standard deviation and vice versa for dimmer ones.

Before training, the individual particles were labeled as either a monomer or oligomer (dimer, trimer, or tetramer). From nanoparticle plasmon coupling simulation during the imaging process, we found that the ratio of dimers to monomers varies from 2−4, and the ratio of trimers to monomers varies from 4−9 for different separations (Supplementary section Figure S1). The counts of monomers to oligomers do approximate these ratios, following a log-normal distribution. This is further shown in Figure 5 (left).

3.2. Model Training. In this section, we describe the architecture and training details of our models. There are two models here: an object detection model for nanoparticle detection and a boosted tree model for classification.

3.2.1. Nanoparticle Detection Model. Our CNN model is a YOLOv8 model, which is state-of-the-art for object detection. It is an improvement on the YOLOv5 model[25,26] and considered SOTA for most tasks that involve classifying an object and bounding its location. The specific architecture of the model is described in Supplementary Section 3 (see details of the YOLOv8Model architecture and Figure S2) and based on ref 27.

Rather than training a model from scratch, we elected to fine-tune an existing model that was pretrained on the COCO data set. This is a transfer-learning-based approach that takes advantage of model weights initialized on an existing object detector and fine-tunes it to detect AuNPs instead. Details on the hyperparameters, batch size, and optimizers are given in Supporting Information Section 3 (see details of the YOLOv8Model Architecture).

The model was trained for up to 200 epochs on a Nvidia RTX 4060 GPU. We used early stopping and found that the model showed no further improvement around approximately 110−150 epochs.

3.2.2. Oligomeric State Classifier. To classify the oligomeric state from spatial and pixel-wise features, we built an extreme gradient-boosted tree model using XGBoost.[28] The learning rate of this model was set to 0.3, the max depth to 20, and the number of estimators to 100. We also built a LightGBM[29] model with a learning rate of 0.02, maximum bins of 15, minimum child samples of 8, and num estimators of 1. These two are state-of-the-art for classification problems.

In both of these models, we optimized the hyperparameters using grid search and used logistic regression as the loss function.

Figure 4 shows the full overview of the process of training both models.

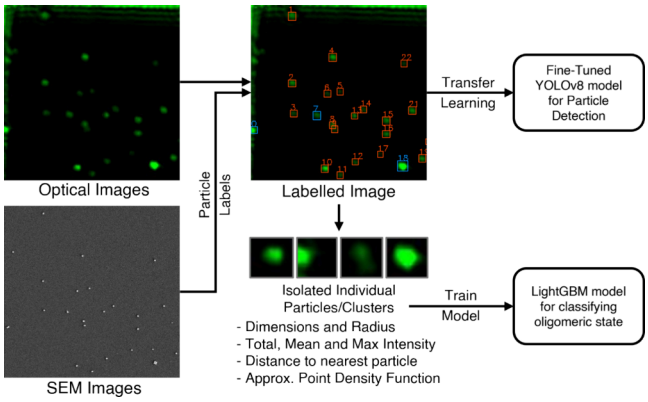

Figure 4. System diagram of the training process. AuNPs embedded in plasmonic random medium samples (in vitro imaging) were captured using confocal laser scattering microscopy (optical images), which was correlated to SEM images. Transfer learning is employed to detect individual particles or clusters, and then, the LightGBM model is used for classifying oligomeric states.

4. EXPERIMENTAL RESULTS

The results of our experimentation are described in this section, divided into nanoparticle detection results and oligomeric state classification results.

4.1. Detecting Particles. For validation purposes, the confidence threshold for the bounding box prediction was set to 0.25. We calculated the precision, recall, and mean average precisions at 0.50 intersection over union (IoU) and 0.95 IoU. The related equations of performance metrics, model training curves, feature weighting, and confusion metrics are shown in Supporting Information Sections 4, 5 (Figures S3−S5) and 6 (Figures S6 and S7), respectively. The validation results are reported as the average results across all eight folds generated by leave-one-out cross-validation. The full results for detecting each particle instance are given in Table 1.

As seen in the table, the model has a precision of 0.943 and a recall of 0.811 on the validation data. We calculate the F1 score to be 0.871, which is a good starting result, especially for such a challenging detection task. Figures S6 and S7 in the Supporting Information show the confusion matrix for this model.

https://doi.org/10.1021/acsomega.4c07914
ACS Omega 2025, 10, 862−870

Table 1. Training and Validation Performance for Fine-Tuning

step	precision	recall	mAP@50	mAP@50:95
Training	0.948	0.926	0.925	0.458
Validation	0.940	0.811	0.854	0.517

Overall, the accuracy of this model, calculated from the true negative and true positive results, is 76.2%.

4.2. Counting and Classifying Particles. For the final classifier, the LightGBM model characterized the oligomeric state with a validation accuracy of 90.0%, while the XGBoost model achieved an accuracy of 87.1%.

This is an excellent result and shows that our pixel-wise features are effective in classifying the oligomeric state. This number is, however, based on our labeled data set, which has very accurate bounding boxes. Since the extraction of pixel-wise features depends on the boxes, poor bounding box localization could lead to lower downstream accuracy.

To validate the results of the full pipeline, we first carry out inference on an image from the correlated optical image data set and then test the results of that with our particle classifier. The results of 8 correlated testing images are given in Table 2. Note that while these images are the source of our training and validation images due to preprocessing and random cropping, none of the original images were seen by the model during the training process.

The true counts of monomers and oligomers were extracted from the SEM image and calculated using ImageJ, but we did not test ImageJ on optical images as it completely failed to distinguish between monomers and oligomers.

In this scenario, the RMSE for counting monomers was 6.245. The RMSE for counting oligomers was 3.62. The MAE for the count of monomers was 4.75, and for oligomers, it was 3.12. The high error rate for detecting oligomers through this approach is expected due to limited data, but monomer detection is highly accurate at 84.9% accuracy.

Weighing the overall accuracy by the average number of monomers and oligomers, we found that the average accuracy of the whole system is 80.7%.

Furthermore, in Figure 5, we display the aggregate histograms for the radii of the detected particles in these images compared to the histograms for the radii from the original test set. While the histograms are not an exact match due to the inaccuracies in our model, the expected log-normal distribution of particle sizes is clearly visible and as expected. This supports our results and shows that the model is working satisfactorily.

This accuracy is a good starting point and may be improved by developing the particle detection model further, using more data, and exploring other possible pixel-wise features.

5. TESTING WITH NONCORRELATED IMAGES

The goal of our work is to find a way to count the number of AuNPs in optical images when there are no correlated SEM images available. As discussed in Section 1, optical imaging has advantages over SEM images, such as higher throughput and speed, lower cost, and a nondestructive nature for live cell imaging.

In this section, we show the results of applying our model in white-light excited optical images, examples of which are given in Figure 3. This step challenges the domain adaptability of our model to different types of microscopy and imaging settings, as well as its basic particle detection and oligomeric state classification abilities.

In order to obtain a comparable set of results, we used ImageJ to detect particles as well. We will discuss the differences between existing "manual" methods and our method. As there are no correlated SEM images available for this test data set, the results from ImageJ should be considered the best measurement from existing methods and form a baseline.

5.1. Time Consumption. Is our method faster? With ImageJ, it took anywhere from half a minute to several minutes to fine-tune the thresholding levels and select optimal filter parameters in order to get an accurate count. Variations in the image, such as the background being lighter than usual or particles being dimmer than usual, can lead to additional processing time.

Additionally, ImageJ does not return results for different types of AuNPs at the same time. Multiple runs of the program with different thresholding and particle size limit settings are needed to count monomers and oligomers.

By contrast, the deep learning model returned results in less than a second, regardless of perturbations in the image.

5.2. Uncorrelated Counting Comparison. Does our method give results comparable to those of ImageJ? To study this, we used our method and ImageJ to count the number of monomers and oligomers in the test data set parallelly. As seen earlier in Figure 2, the monomers and oligomers in these test images are much more distinct compared to the optical images used for training. Therefore, we are able to easily distinguish between the two and note the numbers for counting accurately.

Table 3 shows the results of counting monomers and oligomers for each of the 20 images in this test set. We can see that the mean divergence between our method and ImageJ for

Table 2. Performance Metrics of Correlated Images (Laser-Excited)

	true value from SEM		predicted from optical		percentage error	
image	monomers	oligomers	monomers	oligomers	monomer	oligomers
1	31	5	35 ± 4.5%	5 ± 4.5%	11.4%	0.00%
2	30	4	37 ± 4.5%	6 ± 4.5%	23.3%	50.0%
3	48	4	47 ± 4.5%	3 ± 4.5%	2.12%	25.0%
4	48	4	48 ± 4.5%	1 ± 4.5%	0.00%	75.0%
5	39	5	38 ± 4.5%	2 ± 4.5%	8.00%	60.0%
6	39	5	49 ± 4.5%	1 ± 4.5%	20.4%	80.0%
7	22	7	33 ± 4.5%	2 ± 4.5%	50.0%	71.0%
8	36	4	38 ± 4.5%	9 ± 4.5%	5.26%	55.5%

https://doi.org/10.1021/acsomega.4c07914
ACS Omega 2025, 10, 862−870

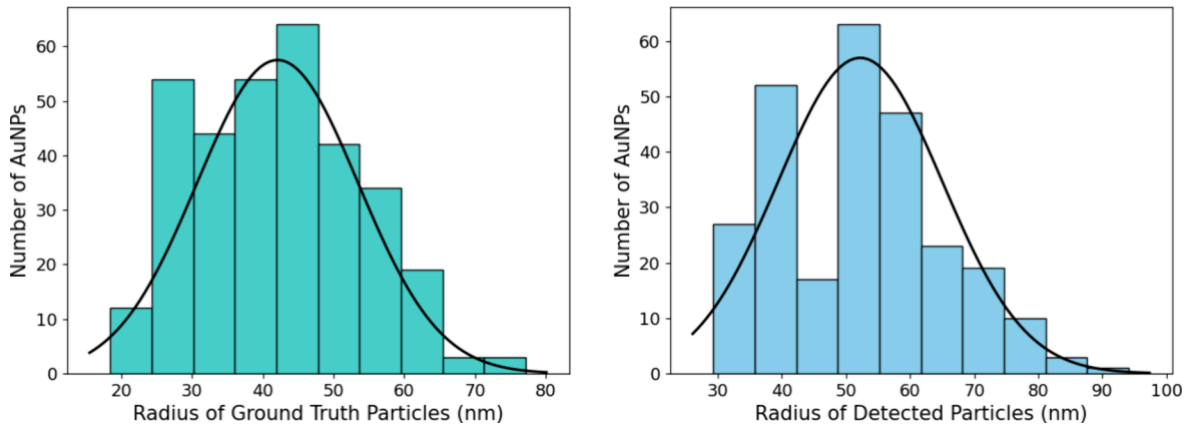

Figure 5. Left—Histogram for particle radii from ground truth data (optical images labeled using correlated SEM images as a basis). Right—Histogram for particle radii predicted by the particle detection model.

Table 3. Counting Monomers and Oligomers in Uncorrelated Images[a]

image no.	monomers	oligomers	our total	imageJ total	divergence
1	191	67	258	285	9.94%
2	223	90	313	217	36.23%
3	228	96	324	247	26.97%
4	220	31	251	250	0.39%
5	231	58	289	236	20.19%
6	416	79	495	300	49.06%
7	239	77	316	288	9.27%
8	205	61	266	239	10.69%
9	237	71	308	244	23.19%
10	127	10	137	157	13.61%
11	260	70	330	298	10.19%
12	231	76	307	308	0.33%
13	192	64	256	297	14.83%
14	206	78	284	239	17.21%
15	193	89	282	256	9.67%
16	233	101	334	259	25.30%
17	172	72	244	236	3.33%
18	165	27	192	209	8.48%
19	109	46	155	186	18.18%
20	128	25	153	195	24.14%

[a]The first three columns show the count from our method.

counting the number of particles is only 16.56% and the median divergence is 14.22%.

Generally, ImageJ tends to count a lower total compared to our method. However, without actually labeling images to serve as a test data set, it is impossible to determine which one is the more accurate method.

5.3. Accuracy in Uncorrelated Images. Is our method empirically more accurate? It is impossible to draw clear conclusions about the accuracy of our methods compared to that of ImageJ without a quantitative comparison. Therefore, we processed the test set of images and labeled them manually by hand.

We limited the labeling to two images due to the time consumption and difficulty of this process. This process is also not as accurate as that of our training set due to a lack of SEM ground truth but still comes close to being an effective comparison.

During the labeling process, we used a heightmap of particle pixel intensities, as shown in Figure 6, to help find all the particles. In the heightmap, the x- and *y*-axes refer to the two-dimensional pixel coordinate, while the *z*-axis shows the intensity of the pixel at the given point in the image. Most monomers show up as small bumps in the surface as they are individual particles, while oligomers are visible as taller spikes due to clustering. In terms of cluster/dimer, the intensity values could be 2−4 times higher compared to monomer

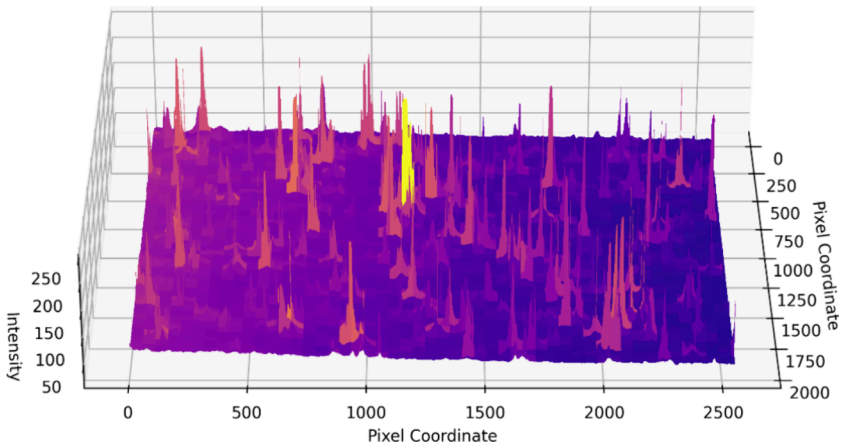

Figure 6. Sample pixel intensity heightmap for an uncorrelated test image. The heightmap is an easy way to visualize the difference between monomers and oligomers.

https://doi.org/10.1021/acsomega.4c07914
ACS Omega 2025, 10, 862−870

intensity, as confirmed by the FDTD simulation shown in the Supplementary section (Figure S1); however, in real experimental scenarios, it could follow a similar pattern.

The bright yellow spike in the middle is likely a trimer or a tetramer, while the rest are dimers. As this is based on pixel size and intensities, factors like light path might have a similar relative impact on the monomer/cluster; however, imaging environment, excitation source, equipment, objectives, lens, and microscope specifications might have a significant impact. The image in Figure 6 does not correspond to any physical or spectroscopic properties of the particles but rather simply the pixels in the final optical image and any clusters present in it.

At the inference time, all pixels with an intensity value lower than or equal to 15 were zeroed out to remove the background. Any pixels with an intensity below 50 had their intensity doubled to improve visibility. Finally, a small Gaussian blur with a 5×5 kernel was used to remove artifacts and sharp edges created by thresholding. These processing steps are effective across all images and do not have to be fine-tuned by hand per image.

We carry out inference using our method and with ImageJ to detect the number of particles. Since ImageJ is unable to distinguish between monomers and oligomers without manual inspection and parameter tuning, we opt to exclude that section of the test and focus on detection. The results are listed in Table 4.

Table 4. Performance Metrics for Detection on Noncorrelated White-Light Excited Images

images	precision	recall	mAP@50	mAP@50:95	F1 score
ImageJ	0.706	**0.797**	N/A	N/A	0.749
our method	**0.847**	0.735	0.762	0.321	**0.783**

The F1 score detecting particles using our method was 0.783. We attribute the lower accuracy here compared with the laser-excited optical images to the extreme dimness of many particles. This can be rectified in future work by using additional training data.

However, ImageJ performs a little worse in detection with an F1 score of 0.749. It does have a high recall, indicating that it is capable of detecting all the correct visible particles in the image, but the low precision indicates that it also detects a lot of false positives—for instance, it might detect a single blurry particle as multiple particles or even detect some noise as a particle since the threshold needs to be set very low to catch the monomers as well. The mAP values are not included, as ImageJ's particle counter does not generate bounding boxes.

Overall, our method is slightly better than other tools like ImageJ in terms of accuracy for detecting particles but is also fully automated with no need for manual setting of thresholds or detection parameters, is much faster, and is capable of distinguishing between monomers and oligomers automatically.

6. CONCLUSIONS

In this study, we designed a novel method to estimate the total number of gold nanoparticles in optical images and determine their oligomeric state. Previous research focused on TEM/SEM images; however, it neglected optical imaging approaches due to randomness and difficulty in analyzing the images. We have demonstrated this is not the case and that deep learning can accurately detect and classify monomers and oligomers from optical microscopy in a nondestructive setting.

We have achieved an accuracy of 76.2% for the detection process and 93.3% for determining the oligomeric state. Overall, the weighted average accuracy of our method is 80.7%. We also compare our results to using ImageJ and find that our method is faster by an order of magnitude and does not require any manual intervention while having either comparable or even much better accuracy depending on the type of optical image.

In the future, we expect to improve the accuracy of our approach significantly. This will require more correlated images for training. Sufficient data will also allow our method to better differentiate distinct higher-order oligomers, such as trimers and tetramers, particularly for densely populated nanoparticle images. While the proposed method was evaluated on spherical-shaped nanoparticles only, we also plan to extend our work to detect the boundaries and analyze other shaped NPs, such as ellipses, dumbbells, bipyramids, triangles, and nanocubes from optical images.

Our deep learning method offers an accurate, efficient, and automated solution for detecting nanoparticles and quantifying oligomerization within polymer matrices using exclusively optical images. We expect that the proposed nondestructive imaging technique will be particularly valuable for assessing nanoparticle uptake and aggregation for studying membrane protein stoichiometry, interactions, and drug delivery in live cells.

■ ASSOCIATED CONTENT

Data Availability Statement

The data underlying this study are available in the published article and its Supporting Information.

Supporting Information

The Supporting Information is available free of charge at https://pubs.acs.org/doi/10.1021/acsomega.4c07914.

Link to code, preparing gold nanospheres for imaging, performance metrics, model training curves and metrics, and confusion matrices (PDF)

■ AUTHOR INFORMATION

Corresponding Author

Abu S. M. Mohsin − *Nanotechnology, IoT and Applied Machine Learning Research Group, BRAC University, Dhaka 1212, Bangladesh*; orcid.org/0000-0001-9281-9088; Email: asm.mohsin@bracu.ac.bd

Author

Shadab H. Choudhury − *Nanotechnology, IoT and Applied Machine Learning Research Group, BRAC University, Dhaka 1212, Bangladesh*

Complete contact information is available at: https://pubs.acs.org/10.1021/acsomega.4c07914

Author Contributions

A.S.M.M. and S.H.C. contributed equally. A.S.M.M. contributed to the conception and design, data collection, analysis and interpretation of results, and manuscript preparation. S.H.C. contributed to data labeling and preprocessing, deep learning model design and training, analysis and interpretation of results, and manuscript preparation.

https://doi.org/10.1021/acsomega.4c07914
ACS Omega 2025, 10, 862−870

Notes

The authors declare no competing financial interest.

■ ACKNOWLEDGMENTS

The authors would like to thank Brac University, Bangladesh, and Swinburne University of Technology, Australia, for research support.

■ REFERENCES

(1) Karim, M. E.; Mohsin, A. S. M. Metasurface absorber based single junction thin film solar cell exceeding 30% efficiency. *Opt. Express* **2024**, *32*, 8214−8229.
(2) Mohsin, A. S. M.; Mobashera, M.; Malik, A.; Rubaiat, M.; Islam, M. Light trapping in thin-film solar cells to enhance the absorption efficiency using FDTD simulation. *J. Opt* **2020**, *49* (4), 523−532.
(3) Mohsin, A. S. *Aggregation and uptake kinetics of gold nanoparticles in biological cells, using plasmon coupling and image correlation spectroscopy*; Swinburne University of Technology: Melbourne, 2015.
(4) Mohsin, A. S. M.; Salim, M. B. Probing the intracellular refractive index and molecular interaction of gold nanoparticles in HeLa cells using single particle spectroscopy. *Int. J. Nanomed.* **2018**, *13*, 6019−6028.
(5) Mohsin, A. S. M.; Ahmed, F. Study the optical property of gold nanoparticles and apply them to design bowtie nanoantenna using FDTD simulation. *J. Opt* **2022**, *51* (3), 543−551.
(6) Mohsin, A. S. M.; Salim, M. B. Probing the Plasmon Coupling, Quantum Yield, and Effects of Tip Geometry of Gold Nanoparticles Using Analytical Models and FDTD Simulation. *IEEE Photonics Journal* **2018**, *10* (3), 1−10.
(7) Okada, T.; Ogura, T. Nanoscale imaging of untreated mammalian cells in a medium with low radiation damage using scanning electron-assisted dielectric microscopy. *Sci. Rep* **2016**, *6* (1), 29169.
(8) Mastrangelo, R.; Okada, T.; Ogura, T.; Ogura, T.; Baglioni, P. Direct observation of the effects of chemical fixation in MNT-1 cells: A SE-ADM and Raman study. *Proc. Natl. Acad. Sci. U. S. A.* **2023**, *120* (51), No. e2308088120.
(9) Palmer, A. G.; Thompson, N. L. Molecular aggregation characterized by high order autocorrelation in fluorescence correlation spectroscopy. *Biophys. J.* **1987**, *52* (2), 257−270.
(10) Petersen, N. O. Scanning fluorescence correlation spectroscopy. I. Theory and simulation of aggregation measurements. *Biophys. J.* **1986**, *49* (4), 809−815.
(11) Mirzaei, M.; Rafsanjani, H. K. An automatic algorithm for determination of the nanoparticles from TEM images using circular hough transform. *Micron* **2017**, *96*, 86−95.
(12) Dahy, G.; Soliman, M. M.; Alshater, H.; Slowik, A.; Ella Hassanien, A. Optimized deep networks for the classification of nanoparticles in scanning electron microscopy imaging. *Comput. Mater. Sci.* **2023**, *223*, No. 112135.
(13) Oktay, A. B.; Gurses, A. Automatic detection, localization and segmentation of nano-particles with deep learning in microscopy images. *Micron* **2019**, *120*, 113−119.
(14) Meng, Y.; Zhang, Z.; Yin, H.; Ma, T. Automatic detection of particle size distribution by image analysis based on local adaptive canny edge detection and modified circular Hough transform. *Micron* **2018**, *106*, 34−41.
(15) Schneider, C. A.; Rasband, W. S.; Eliceiri, K. W. NIH Image to ImageJ: 25 years of image analysis. *Nat. Methods* **2012**, *9* (7), 671−675.
(16) Qu, E. Z.; Jimenez, A. M.; Kumar, S. K.; Zhang, K. Quantifying Nanoparticle Assembly States in a Polymer Matrix through Deep Learning. *Macromolecules* **2021**, *54* (7), 3034−3040.
(17) Nartova, A. V.; Mashukov, M. Y.; Astakhov, R. R.; Kudinov, V. Y.; Matveev, A. V.; Okunev, A. G. Particle Recognition on Transmission Electron Microscopy Images Using Computer Vision and Deep Learning for Catalytic Applications. *Catalysts* **2022**, *12* (2), 135.
(18) Okunev, A. G.; Mashukov, M. Y.; Nartova, A. V.; Matveev, A. V. Nanoparticle Recognition on Scanning Probe Microscopy Images Using Computer Vision and Deep Learning. *Nanomaterials (Basel)* **2020**, *10* (7), 1285.
(19) López Gutiérrez, J. D.; Abundez Barrera, I. M.; Torres Gómez, N. Nanoparticle Detection on SEM Images Using a Neural Network and Semi-Synthetic Training Data. *Nanomaterials (Basel)* **2022**, *12* (11), 1818.
(20) Kaphle, A.; et al. Deep Learning-Based TEM Image Analysis for Fully Automated Detection of Gold Nanoparticles Internalized Within Tumor Cell. *Microscopy and Microanalysis* **2023**, *29* (4), 1474−1487.
(21) Monchot, P. Deep Learning Based Instance Segmentation of Titanium Dioxide Particles in the Form of Agglomerates in Scanning Electron Microscopy. *Nanomaterials (Basel)* **2021**, *11* (4), 968.
(22) Melanthota, S. K.; Gopal, D.; Chakrabarti, S.; Kashyap, A. A.; Radhakrishnan, R.; Mazumder, N. Deep learning-based image processing in optical microscopy. *Biophys Rev.* **2022**, *14* (2), 463−481.
(23) Xu, Y.; et al. Machine Learning Enhanced Optical Microscopy for the Rapid Morphology Characterization of Silver Nanoparticles. *ACS Appl. Mater. Interfaces* **2023**, *15* (14), 18244−18251.
(24) Mohsin, A. S. M.; Choudhury, S. H. Label-free quantification of gold nanoparticles at the single-cell level using a multi-column convolutional neural network (MC-CNN). *Analyst* **2024**, *149* (8), 2412−2419.
(25) Jocher, G.et al.*ultralytics/yolov5: v7.0 - YOLOv5 SOTA Real Time Instance Segmentation*; Zenodo, 2022.
(26) Terven, J.; Cordova-Esparza, D. A Comprehensive Review of YOLO Architectures in Computer Vision: From YOLOv1 to YOLOv8 and YOLO-NAS. *Mach. Learn. Knowl. Extr.* **2023**, *5* (4), 1680−1716.
(27) RangeKing (https://github.com/RangeKing), *Brief summary of YOLOv8 model structure · Issue #189 · ultralytics/ultralytics*, GitHub. Available: https://github.com/ultralytics/ultralytics/issues/189. Accessed: Jun. 15, 2024. [Online].
(28) Chen, T.; Guestrin, C. XGBoost: A Scalable Tree Boosting System, in *Proceedings of the 22nd ACM SIGKDD International Conference on Knowledge Discovery and Data Mining*; ACM: San Francisco California USA, 2016; 785−794.
(29) Ke, G. LightGBM: A Highly Efficient Gradient Boosting Decision Tree, in *Advances in Neural Information Processing Systems*; Curran Associates, Inc., 2017. Available: https://proceedings.neurips.cc/paper/2017/hash/6449f44a102fde848669bdd9eb6b76fa-Abstract.html. Accessed: Jun. 15, 2024. [Online].

https://doi.org/10.1021/acsomega.4c07914
ACS Omega 2025, 10, 862−870